ACS APPLIED MATERIALS & INTERFACES

Research Article

www.acsami.org

Silver Nanowire Network Transparent Electrodes with Highly Enhanced Flexibility by Welding for Application in Flexible Organic Light-Emitting Diodes

Hahn-Gil Cheong,[†] Ross. E. Triambulo,[†] Gun-Hwan Lee,[‡] In-Sook Yi,[§] and Jin-Woo Park*[,†]

[†]Department of Materials Science and Engineering, Yonsei University, Seoul 120-749, Korea

[‡]Advanced Thin Film Research Group, Korea Institute of Materials Science, Changwon 642-831, Korea

[§]R&D Center, InkTec Co., Ltd., Ansan 425-839, Korea

ABSTRACT: We present highly flexible Ag nanowire (AgNW) networks welded with transparent conductive oxide (TCO) for use in electrical interconnects in flexible and wearable electronic devices. The hybrid transparent conductive electrodes (TCEs) produced on polymer substrates consist of AgNW networks and TCO that is deposited atop the AgNWs. The TCO firmly welds the AgNWs together at the junctions and the AgNWs to the polymer substrates. Transmission electron microscopy (TEM) analysis show that TCO atop and near AgNWs grows as crystalline because AgNWs act as crystalline seeds, but the crystallinity of the matrix TCO can be controlled by sputtering conditions. The sheet resistances (R_s) of hybrid TCEs are less than the AgNW networks because junction resistance is significantly reduced due to welding by TCO. The effect of welding on decreasing R_s is enhanced with increasing matrix crystallinity, as the adhesion between AgNWs and TCO is improved. Furthermore, the bending stability of the hybrid TCEs are almost equivalent to and better than AgNW networks in static and cyclic bending tests, respectively. Flexible organic light-emitting diodes (f-OLEDs) are successfully fabricated on the hybrid TCEs without top-coats and the performances of f-OLEDs on hybrid TCEs are almost equivalent to those on commercial TCO, which supports replacing indium tin oxide (ITO) with the hybrid TCEs in flexible electronics applications.

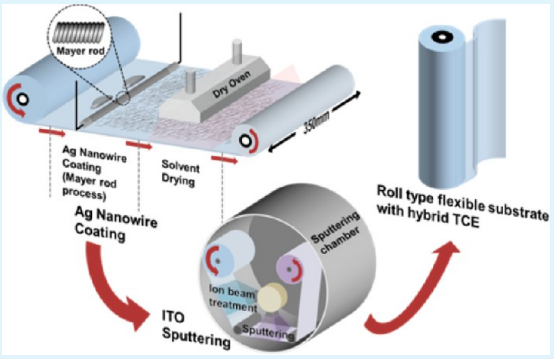

KEYWORDS: *transparent conductive electrode, flexible OLED, interface, Ag nanowires, ITO*

1. INTRODUCTION

Transparent conductive oxides (TCOs) are commonly used for electrical interconnections in various photovoltaic devices and displays.[1−3] Indium tin oxide (ITO) is the most extensively used TCO, particularly in displays, because its optical and electrical properties are superior to those of other TCO materials.[4−6] However, the increasing cost of ITO as a result of indium scarcity must be addressed, and new materials are needed to replace ITO.[7] In addition, ITO's brittleness and incompatibility with other biomaterials because of indium toxicity have become critical issues because of the application of ITO in electrodes for flexible electronics such as flexible displays and wearable devices.[7,8]

Various materials, ranging from multilayer composite films to networks of one- or two-dimensional materials such as graphene,[9−11] nanotubes,[12,13] and metal nanowires,[14−19] have been investigated as ITO replacements. The suggested materials have greater flexibility on polymer substrates than does ITO. However, some of the materials such as carbon nanotube networks and graphene exhibit electrical and optical properties that are inferior to those of ITO.[9] Among the replacement candidates, AgNWs have become the most promising candidates because they not only have greater functional and mechanical properties than ITO but also can be coated onto large-area flexible polymer substrates using new solution coating technologies.[20,21]

Together with the superior advantages compared with ITO, drawbacks have also been revealed, such as electrical shorts at the ends of disconnected wires[22] and nonuniform functionalities over large areas, reducing the reproducibility of devices. Because of these limitations of AgNWs, the use of top coatings has been required. However, top-coats often degrade the functional properties of networked films.[23] A composite-type transparent conductive electrode (TCE) has been proposed as an alternative to the ultrathin TCE materials with high aspect ratios. Among hybrid TCEs, TCO/metal/TCO composite-structured TCEs have been extensively studied.[24,25]

The metals in the composite are either continuous films or networks of NWs. However, the increased fabrication complexity would increase manufacturing costs, limiting the application of these composites to large-area displays. In addition, during the lag time between fabrication steps, the underlying TCO

Received: February 24, 2014
Accepted: April 10, 2014
Published: April 10, 2014

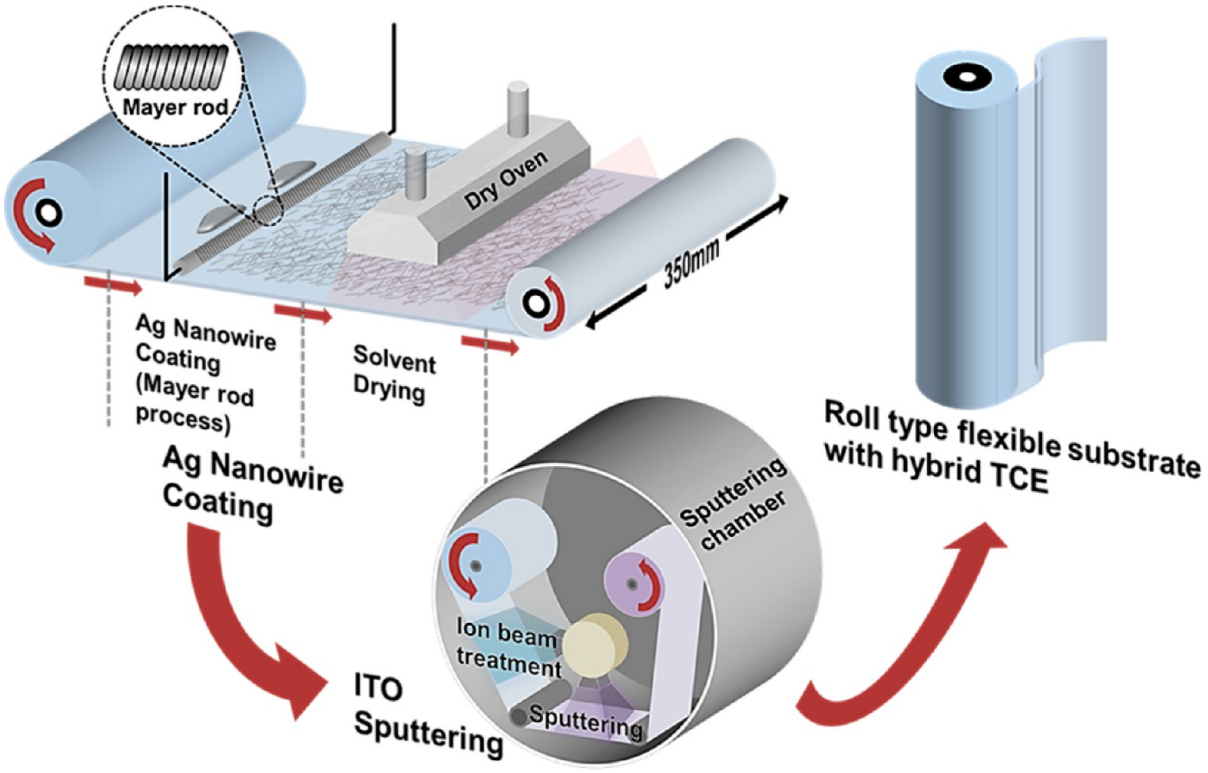

Figure 1. Schematic description of the roll-to-roll coating process for constructing the hybrid TCEs.

layer is exposed to contaminants, such as solvents from the wet processing, which might be detrimental to the overall properties of the electrode. Moreover, application of the composite TCE to optoelectronic devices on polymer substrates has not yet been successful.

To resolve these issues, we have investigated composite films of AgNW networks with conductive polymers such as PETDOT:PSS. However, the polymer matrix between the AgNWs rather degrades the lifetime of OLEDs,[26] and further improvements in processes are also needed to produce large-area films with uniform properties. Localized heating techniques, such as light-induced plasmonic nanowelding, have been developed to produce large interconnected nanowire networks by junction welding without damaging the plastic substrates.[27] Using this method, non-uniformity in electrical resistance has been highly improved; however, the surface roughness that prevents sufficient contact with polymer layers of devices is still unresolved.[27]

In this study, we develop a hybrid TCE consisting of AgNWs coated on PET using the Mayer rod method and TCO deposited on the AgNWs using DC magnetron sputtering. Herein, TCO is an auxiliary material that welds the AgNWs at junctions and the AgNWs into the substrates, which is expected to reduce the contact resistances and to improve flexibility. In this study, ITO is selected as the TCO because the process−microstructure−property relationships of ITO are known better than any other TCO materials. Hence, the microstructure−property relationships found in this study can be extended to hybrid TCEs with other TCO materials.

The coating processes have been successfully applied to roll-to-roll processes, yielding roll-type large area flexible substrates (350 mm wide by 500−-1000 m long), as schematically illustrated in Figure 1. For the flexible polymer substrate, we selected PET. Because commercial roll-type PET substrates with ITO are available as reference materials, we selected ITO as the matrix material. The ITO thickness (h_f) was less than a third of that of commercial TCO on PET.

The bending stability of the hybrid TCE was tested and compared with AgNWs and homogeneous ITO. By analyzing the microstructures of the hybrid TCEs before and after bending tests, the cracking mechanism of the TCE is elucidated, and optimum structures to further increase flexibility are suggested. Finally, f-OLEDs are fabricated on the hybrid TCE to confirm the applicability to real devices for which previously developed ITO replacements could not be used.

2. EXPERIMENTAL PROCEDURES

The thickness of PET is 120 μm and no primer layer was coated on PET. ITO thin films were deposited atop PET with Ag nanowires. These processes are well-developed; therefore, a commercial roll-type product (350 mm width by 500−1000 m long) can be produced. Atop the PET substrate, AgNWs (diameter, 30−40 nm; length, 20−30 μm, from Nanopyxis) were coated using the Mayer-rod process using various AgNW solutions to achieve 30 Ω/□ and 80 Ω/□ (with AgNW surface area coverage of approximately 8.4% and 9.5%, respectively). Then, 30 and 50 nm ITO (from Advanced Nano Products, Deajun, Korea) thin films were deposited using a DC magnetron sputtering system under fixed conditions (power = 50 W, Ar flow rate = 70 sccm, O_2 flow rate = 0.1 sccm) except for the substrate temperature.

Mostly *c*-ITO films were deposited at a 75 °C substrate temperature, whereas mostly *a*-ITO films were deposited at substrate temperatures <35 °C. Specimens for material analysis were randomly cut from the rolls with functional coatings. Using AFM, the surface morphology of the coatings was determined. Using GAXRD, FE-SEM, and HR-TEM, the microstructure and the degree of crystallinity of the ITO on the AgNWs were analyzed. The optical transmittance in the visible range (wavelength = 380−750 nm) and R_s of the hybrid TCEs

were determined using UV−visible spectroscopy and a 4 point probe, respectively.

To verify the bending stability of the hybrid TCEs, we performed static and cyclic bending tests using a cyclic bending tester. Detailed descriptions of the tester and testing procedures can be found elsewhere.[28] The samples were bent to a bending radius of as high as 1 mm using a 1 mm s^{-1} bending rate for the static bending test. Using the same bending machine, the cyclic bending test samples were bent for 10 000 cycles at a 5 mm bending radius at a 80 mm s^{-1} bending rate. Measurements of the change in R_s were performed in situ during the bending test.

f-OLEDs were fabricated on top of the hybrid TCEs. The f-OLEDs consisted of five layers, as illustrated in Figure 8a. PEDOT:PSS (Heraeus Clavios PH 500) was coated as a hole transfer layer (HTL) using the spin coating process (1500 rpm). Then, in a N_2 gas filled glove box, an emission layer (EL), 1.0 wt % solution of active red polymer (livilux by Merck) in toluene, was spin-coated (2000 rpm) on top of the HTL. Before each spin-coating process, the surfaces were O_2 plasma-treated (140 W, 90 s).

After each coating step of the HTL and EL, the samples were heated at 115 °C for 1 h. Electron transport material (ETM) cesium carbonate (Sigma-Aldrich), Cs_2CO_3, in 0.5 wt % solution with 2-ethoxyethanol was spin coated at 3000 rpm atop the EL and heat treated at 115 °C for 20 min. Then, a 100 nm Al cathode was deposited on top of the ETM using a thermal evaporator. Using a Keithley 2400 source meter and Minolta CS-200 chroma meter, the J (current density) $-V$ (voltage) and L (luminance)$-V$ curves of the f-OLED were generated.

3. RESULTS AND DISCUSSION

Detailed sample descriptions are summarized in Table 1. In this table, the inclusion of *a* and *c* in the sample names indicates that the ITO was deposited under the conditions previously optimized[27] for growing mostly amorphous ITO (*a*-ITO) and mostly *c*-ITO, respectively. H in the sample names is an abbreviation for "hybrid". The PET was coated with AgNW networks of two different densities. The PETs coated with the high- or low-density AgNWs, which were randomly selected and cut from the rolls, are shown in Figure 2a and b, respectively. The substrate with the higher density AgNWs (Ag3 in Table 1) has a smaller R_s, which is almost one third that of Ag8. As observed in Figure 2c−f, the ITO is uniformly coated on the AgNWs and PET.

Table 1. Detailed Sample Descriptions

sample name	R_s of bare AgNW layer (Ω/□)	ITO deposition temperature (°C)	ITO thickness (nm)
*a*30		>35	30
*a*50			50
*c*30		75	30
*c*50			50
Ag3	30		
H3*a*30		>35	30
H3*a*50			50
H3*c*30		75	30
H3*c*50			50
Ag8	80		
H8*a*30		>35	30
H8*a*50			50
H8*c*30		75	30
H8*c*50			50

The surface morphologies of Ag3, H3*a*30, and H3*a*50 are compared in Figure 2g. Typical atomic force microscopy (AFM) surface profiles of bare AgNWs and hybrid TCEs are presented in Figure 2g-left images for Ag3 and H3*a*30. From the line scan of NWs, as indicated in the H3*a*30 AFM image, the average peak-to-valley roughness (R_{P-V}) of the samples was determined from at least eight measurements. Ag3, H3*a*30, and H3*a*50 have similar R_{P-V}s of 36.3, 40.4, and 38.5 nm, respectively. Together with the cross-sectional views of the line profiles in Figure 2g-right images, these results suggest that the surface morphology of the AgNW coatings is reflected on the surface of ITO and that the ITO coatings are uniformly coated atop the AgNWs. This means that the tips of disconnected wires will not directly contact the polymer layers coated on the electrode films, which will prevent electrical shorts at the ends of disconnected AgNWs.

The glancing angle X-ray diffraction (GAXRD) analysis results for *a*50 and *c*50 (Figure 3a) confirm that the two deposition conditions described in the experimental section and Table 1 are optimized for growing *a*-ITO and *c*-ITO, respectively. According to Figure 3a, the major preferred growth orientation of AgNWs is (111). The large peak from 20 to 30° 2θ in panels a and b in Figure 3 corresponds to PET. As shown in Figure 3b, the overall crystallinity of ITO in the hybrid TCEs is mainly controlled by the deposition conditions, although the AgNWs can act as crystalline seeds.

In Figure 3b, it is clearly visible that the degrees of crystallinity of ITO in the H3*c* series hybrid TCEs are enhanced compared with the H3*a* series despite the ITO peaks being partially merged into the large PET peak. To present the small peaks clearly, we separated the large peak of PET from others using software equipped in GAXRD. The peak separation data is presented in Figure 3c. Similar degrees of crystallinity to the H3*c* - series in Figure 3b and 3c were obtained for the H8*c* series. As shown in panels b and c in Figure 3, (222) is the most preferred growth orientation of ITO in H3*c*30 and H3*c*50. (400), (440), and (622) peaks also appeared in H3*c*50. Generally, the crystallinity of the ITO films improves with increasing h_i, as shown in Figure 3b.[29]

The high-resolution TEM (HR-TEM) analysis results in Figure 4a−d reveal that the ITOs deposited atop and near the AgNWs always grow crystalline. This phenomenon appears to be affected by the AgNWs, which act as crystalline seed layers (see the schematic description in Figure 4e). Hence, variations in the degrees of crystallinity and in the preferred growth orientations of ITO from the AgNWs through the matrix occur. On the basis of the bright-field TEM images, selected area diffraction pattern (SADP), and fast Fourier transforms (FFT) of the HR-TEM images in Figure 4a, the matrix of H3*a*30 is mostly amorphous (S1 and F1). FFT analysis in F1 and F2 reveal that ITO grown on top of and near the AgNWs is most preferentially along the (222), (400), and (440) orientations.

Unlike H3*a*30, crystalline nuclei of ITO are visible in the matrix of H3*c*30, which is confirmed in S2 and S3 in Figure 4b. Indexing the diffraction spots in S2 and S3 was not possible; however, most of the nuclei are expected to be along the (222) orientation based on the GAXRD results (presented in Figure 3b). F3 and F4 indicate that the major growth orientations of ITO on AgNWs are the same as those in H3*a*30; however, a slight variation in the orientations occurs closer to the ITO matrix.

Figure 4c reveals that the matrix of H3*a*50 remains mostly amorphous, similar to H3*a*30. However, S4 and S5 indicate that a small number of *c*-ITO nuclei are formed in the matrix. The crystalline nuclei appearing in the matrix of H3*c*30 (S2 and S3 in Figure 4b) grow to form grains as h_f is increased in H3*c*50

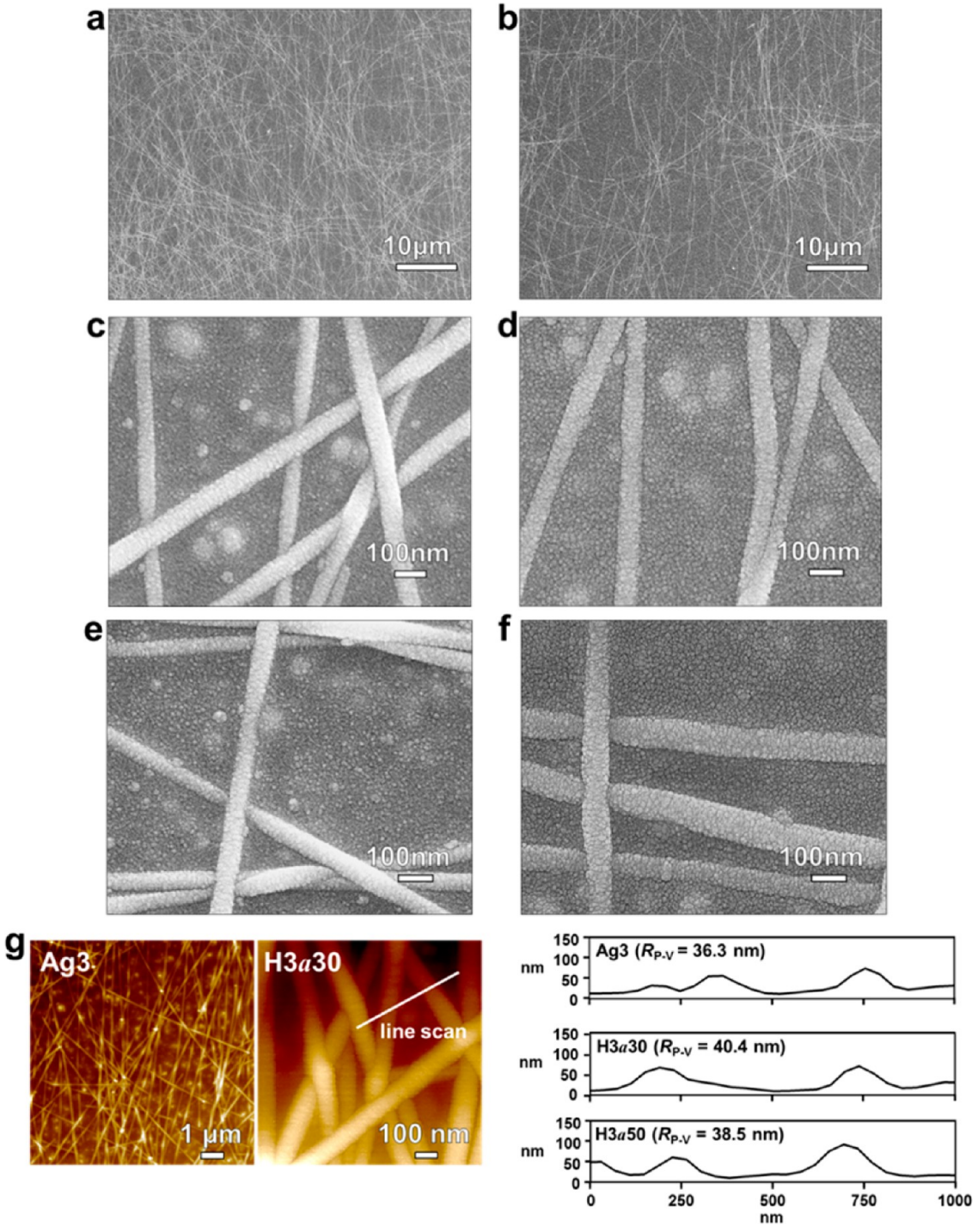

Figure 2. FE-SEM surface images of (a) Ag3, (b) Ag8, (c) H3*a*30, (d) H3*a*50, (e) H3*c*30, and (f) H3*c*50. AFM (g, left) surface scan images and (g, right) line scan cross-section views of AFM images with the average peak-to-valley surface roughness (R_{P-V}) indicated in parentheses.

according to the bright-field images of Figure 4d. Compared with S2 and S3 in Figure 4b, there is an increase in both the number and intensity of the diffraction spots in S6 to S8. On the basis of F2−F7, (222), (400), and (440) are the preferred growth orientations of ITO around AgNWs, and the (131) orientation additionally appeared in the matrix ITO as in the *c*-ITO near AgNWs in H3*c*30. The microstructures of the samples in Figure 4a−d are schematically described in Figure 4e for better understanding.

As shown in Table 2, R_s of Ag3 is almost an order of magnitude smaller than that of the homogeneous ITOs, and the average and maximum optical transparency (T) values, which are T_{ave} and T_{max}, respectively, of Ag3 and Ag8 are equivalent to those of 30 nm ITO and are better than that of 50 nm ITO. In the data of T in Table 2, the reflective losses from the substrate were considered. Therefore, T_{ave} of the Samples in Table 2 are increased by 7−9% when the loss by substrate is excluded. Haze of Ag3 and Ag8 in Table 1 is 2% on average. In hybrid TCEs in Table 2, haze was increased by 0.4%, which is almost negligible.

The R_s of the hybrid TCEs are less than those of the AgNW networks (Ag3 and Ag8). In the hybrids with Ag3 (a higher

dx.doi.org/10.1021/am5011354 | ACS Appl. Mater. Interfaces 2014, 6, 7846−7855

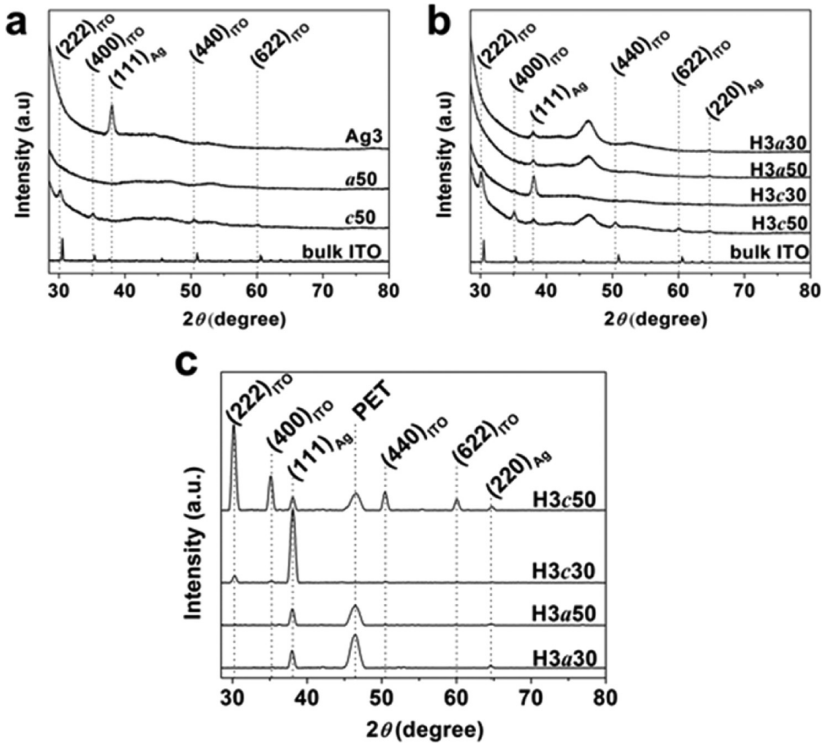

Figure 3. GAXRD (0.5° incident angle) analysis results for (a) *a*50, *c*50, and Ag3; and (b) H3*a*30, H3*a*50, H3*c*30, and H3*c*50; (c) GAXRD data of H3*a*30, H3*a*50, H3*c*30, and H3*c*50, where the large PET peak at 22° was separated from other peaks for clear presentation of small peaks such as $(222)_{ITO}$ of H3*c*30.

density network), R_s decreases by 6.7 to 22.7 %. The decreases in R_s are greater in the H8-series samples and reach a maximum of almost 50 % in H8*c*50 compared with Ag8 (Table 2). In contrast to R_s, T_{ave} of the hybrid TCEs is lower than that of the AgNW networks. However, decreases in T_{max} of the hybrid TCEs compared with the AgNW networks are almost negligible. Both T_{ave} and T_{max} are decreased further upon increasing h_f, following the general relationship between h_f and T.[30] The industry standards for R_s and T of TCEs for OLEDs in display applications are known to be 15 Ω/□ and 95% (when the reflective loss by the substrate is excluded), respectively.

The outer bending test results of the hybrid TCEs are compared with the homogeneous ITO and AgNW networks in Figure 5. There is little change in R_s of Ag3 and Ag8 down to 1 mm bending radius (r_b). In contrast, the homogenous ITO becomes an insulator between 5.5 mm and 3.5 mm r_b. On the basis of Figure 5a, the homogenous ITO is stronger as the film becomes thinner and crystalline, as can be easily predicted from our previous studies.[29] Hence, *c*30 is the most stable at bending, and *a*50 is the weakest among the homogeneous ITO samples, as indicated in Figure 5a.

On the basis of the test results in panels b and c in Figure 5, the bending stability of the hybrid TCEs is significantly better than that of the homogeneous ITO. In particular, when h_f is 30 nm, the bending stability of the hybrid TCEs is almost equivalent to that of Ag3 and Ag8. When h_f is increased to 50 nm, the effect of the ITO crystallinity on the bending stability of the hybrid TCEs is clearly visible. Using the critical bending radius (r_b^{crit}) below which the change in R_s becomes larger than 10% as a metric to compare the bending stability,[26] r_b^{crit} of H3*a*50 and H8*a*50 is 4.5 and 4 mm, respectively; however, r_b^{crit} of H3*c*50 and H8*c*50 is 3.5 mm (Figure 5a, b).

When h_f is 30 nm, r_b^{crit} of the hybrid TCEs becomes 1.5−2.5 mm. In the hybrid TCEs with *a*-ITO matrix, the effect of the wire density on the bending stability seems to be negligible (Figure 5b). However, it is noticeable that, when the matrix is *c*-ITO, the TCE with denser AgNW networks is more stable in bending at a fixed h_f according to Figure 3c. According to the test results in Figure 5b, c, H3*c*50 and H3*c*50 appeared to be the most stable under static outer bending tests among the hybrid TCEs and are almost as stable as AgNW networks. H3*a*50 is the weakest. The effects of ITO crystallinity on the bending stability shown in Figure 5b, c can be explained by the results of field emission-scanning electron microscopy (FE-SEM) analysis about the structural changes caused by the bending test in Figure 6a−f.

According to the FE-SEM analysis, the modes of cracking depend on the crystallinity of the matrix ITO similar to r_b^{crit}. The ITO in H3*c*30 has an improved degree of crystallinity compared with H3*a*30 but ITO films except for those interfacing with AgNWs remains mostly amorphous (Figure 4 b). Hence, H3*c*30 exhibits a similar mode of cracking to H3*a*30. As presented in Figure 6a, b, the brittle cracks appear to be initiated in ITO and to propagate across the ITO matrix, breaking the wires along the direction perpendicular to the tension induced by bending,[31] which increases R_s of the hybrid TCEs.

However, the crack path is somewhat zigzagged in H3*a*30 and H3*c*30 because the cracks propagate preferentially along the interfaces between ITO and AgNWs, while breaking the wires when the crack initiated in ITO encounters the AgNWs (Figure 6a and b). The interfacial cracks in H3*a*30 and H3*c*30 are shown in Figure 6e, f, respectively. In H3*a*50, a similar zigzag mode of crack propagation to H3*a*30 and H3*c*30 is observed, as shown in Figure 6c. However, the interfacial crack

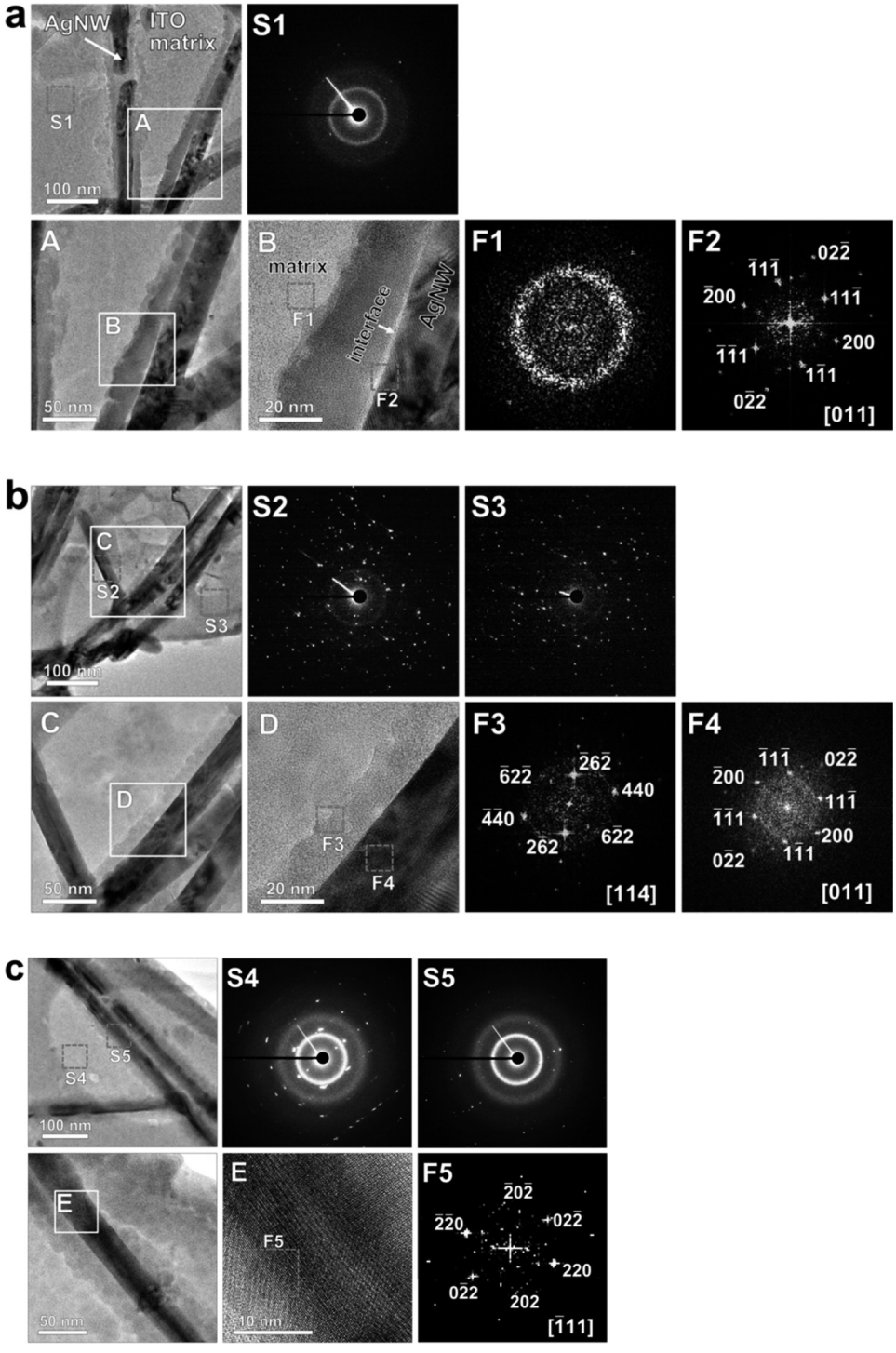

Figure 4. continued

dx.doi.org/10.1021/am5011354 | *ACS Appl. Mater. Interfaces* 2014, 6, 7846−7855

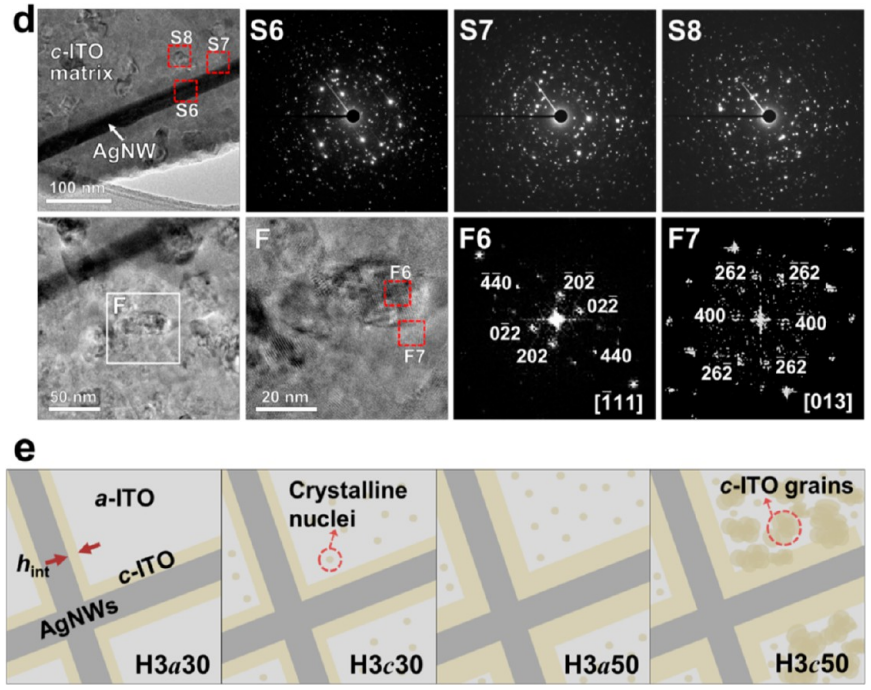

Figure 4. Plan-view HR TEM analysis results with bright-field images, SADP, and FFTs for (a) H3*a*30, (b) H3*c*30, (c) H3*a*50, and (d) H3*c*50, and (e) schematic images describing and summarizing the HR TEM analysis results for the hybrid TCEs in a–d.

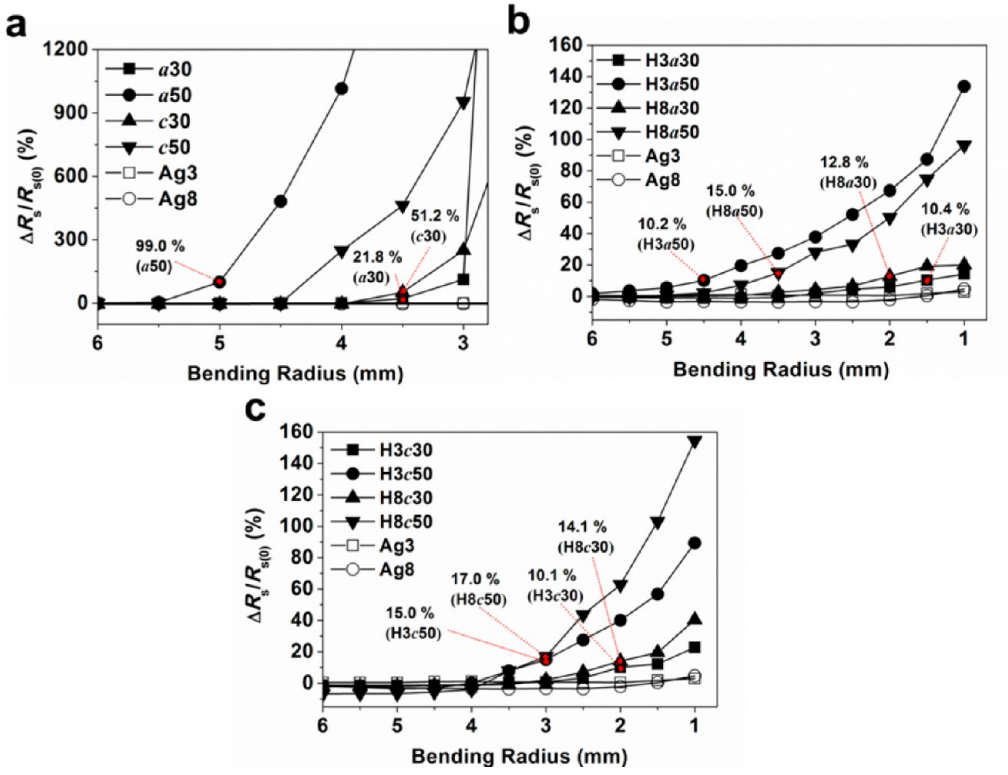

Figure 5. Static outer bending test results for (a) Ag3 and Ag8 compared with *a*30, *a*50, *c*30, and *c*50; (b) H3*a*30, H3*a*50, H8*a*30, and H8*a*50 compared with Ag3 and Ag8; and (c) H3*c*30, H3*c*50, H8*c*30, and H8*c*50 compared with Ag3 and Ag8 ($R_{s(0)}$ is initial sheet resistance before bending test).

propagation is significantly reduced in H3*c*50 compared with H3*a*50, as shown in Figure 6d.

In H3c50, the cracks propagate through the films by breaking the AgNWs rather than circle around the wires along the interfaces. Hence, the crack path becomes straighter than H3*a*50, as observed in Figure 6d. This propagation trend indicates that the adhesion strength between the ITO and AgNWs becomes significantly enhanced as the crystallinity is improved in H3*c*50 compared with H3*a*30, H3*c*30, and H3*a*50. In addition, this finding explains why R_s of H8*c*50 is increased

dx.doi.org/10.1021/am5011354 | ACS Appl. Mater. Interfaces 2014, 6, 7846–7855

Table 2. Electrical and Optical Properties of the Samples in Table 1

sample name	sheet resistance (Ω/□)	average T (T_{ave}) (%)	Maximum T (T_{max}) [%]
*a*30	291.2	86.4	92.0
*a*50	147.5	74.9	82.5
*c*30	294.1	81.6	86.8
*c*50	255.6	77.3	85.8
Ag3	30.0	87.3	89.8
H3*a*30	27.8	79.5	88.1
H3*a*50	23.2	71.1	82.0
H3*c*30	24.2	79.8	87.6
H3*c*50	28.0	72.0	83.4
Ag8	80.0	89.1	90.9
H8*a*30	64.5	82.7	90.2
H8*a*50	52.6	74.5	84.3
H8*c*30	50.1	87.3	89.8
H8*c*50	45.5	73.2	83.6

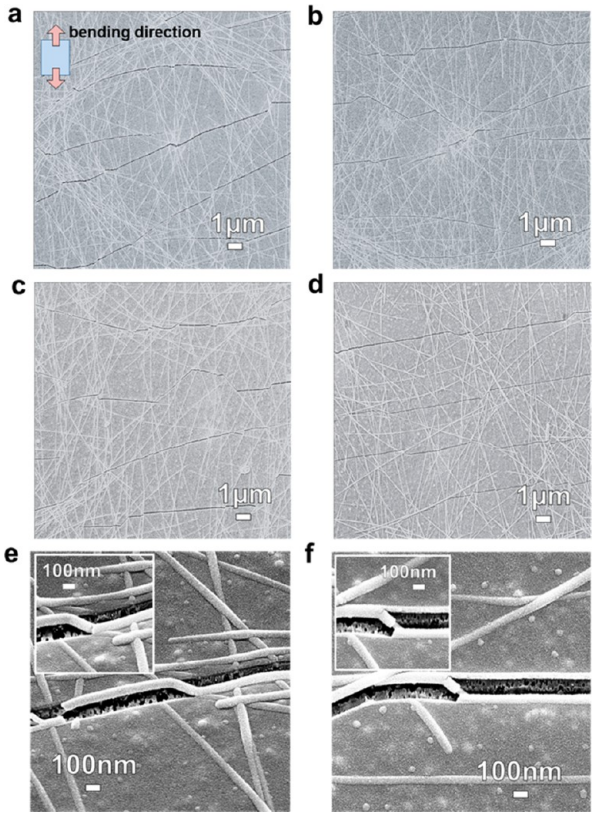

Figure 6. Low-magnification FE-SEM images showing the crack propagation patterns at 2 mm - r_b in (a) H3*a*30, (b) H3*c*30, (c) H3*a*50, and (d) H3*c*50, and high-magnification images of (e) H3*a*30 and (f) H3*c*30 for the same r_b as a.

to a larger degree than H3*c*50, H3*a*50, and H8*a*50 at r_b less than 2 mm in Figure 5b, c. As the ITO matrix becomes stiffer with increasing h_f and the adhesion strength improves with the degrees of ITO crystallinity, more wires are likely to be broken on ITO cracking.

Cyclic bending tests of the hybrid TCEs were performed at a fixed r_b of 5 mm for 10 000 cycles, which is an industrial standard to evaluate the bending stability of TCEs. The test results are summarized in Figure 7. According to Figure 7, the changes in R_s of H3*a*50 and H3*c*50 are greater than 10% at

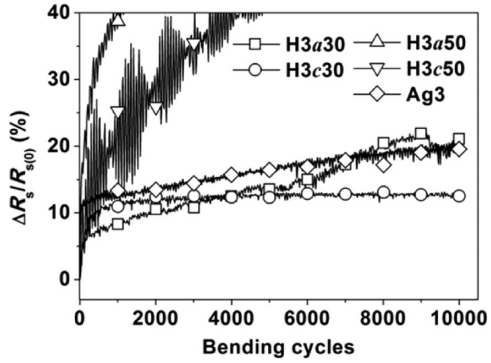

Figure 7. Cyclic outer bending test results at r_b = 5 mm for Ag3, H3*a*30, H3*c*30, H3*a*50, and H3*c*50.

fewer than 100 cycles, and the deviations between the cycles are large and change continuously. It should be noted that H3*c*30 is the most stable under cyclic bending among the samples and is even more stable than Ag3. Although R_s of Ag3 and H3*a*30 continues to increase with increasing cycles, R_s of H3*c*30 increases by 10% until 1000 cycles and is maintained up to 10 000 cycles, as demonstrated in Figure 7. FE-SEM analysis was also performed, and the results confirmed that no noticeable change in the microstructures of the hybrid films after cyclic testing was observed. 10% increase in the R_s is about 3 Ω/□, which is as small as the standard deviation of the sheet resistances of PET coated with AgNW networks. The adhesion between wires at the junctions seems to become loose under the bending as many as 10,000 cycles, which may cause the increase in R_s.

Figure 8a illustrates the structures of f-OLEDs, and the $J-V$ and $L-V$ curves of the f-OLEDs on H3*a*30 and H3*c*30 are presented in panels b and c in Figure 8, respectively. For the comparison, we fabricated f-OLEDs on AgNW networks without top-coats, but the f-OLEDs were not lit. From Figure 8b, it can be observed that the $J-V$ characteristics of f-OLEDs on the hybrid TCEs are equivalent to those on commercially available, homogeneous 100−150 nm ITO on glass substrates.[22,32] Furthermore, the $J-V$ characteristics are significantly better than those of f-OLEDs on AgNW.[22]

Especially, $L-V$ characteristics of the f-OLEDs in Figure 8c are promising results, confirming the possibility of ITO replacement with the hybrid TCEs developed in this study. As far as the authors know, the light output of f-OLEDs on hybrid TCEs with AgNWs has not been reported. Increasing V, more light output was measured in f-OLEDs on H3*c*30 than on H3*a*30 according to Figure 8c, which reveals that the ITO crystallinity and interfacial structures between nanowires and ITO affect the optical properties and carrier transport characteristics of hybrid TCEs as well as the mechanical strength. Combined with the excellent bending stability presented in Figure 7, the results in Figure 8b and c suggest that hybrid TCEs are better suited than homogeneous ITO and AgNWs for the anodes of f-OLEDs.

4. CONCLUSION

In this study, we developed metal-oxide hybrid TCEs with significantly better bending stability than commercial ITO and even AgNW networks that have been considered to be the next-generation TCEs for replacing ITO. The uniformly deposited ITO between and atop the AgNWs appears to yield excellent welding of the wire junctions and AgNWs to the

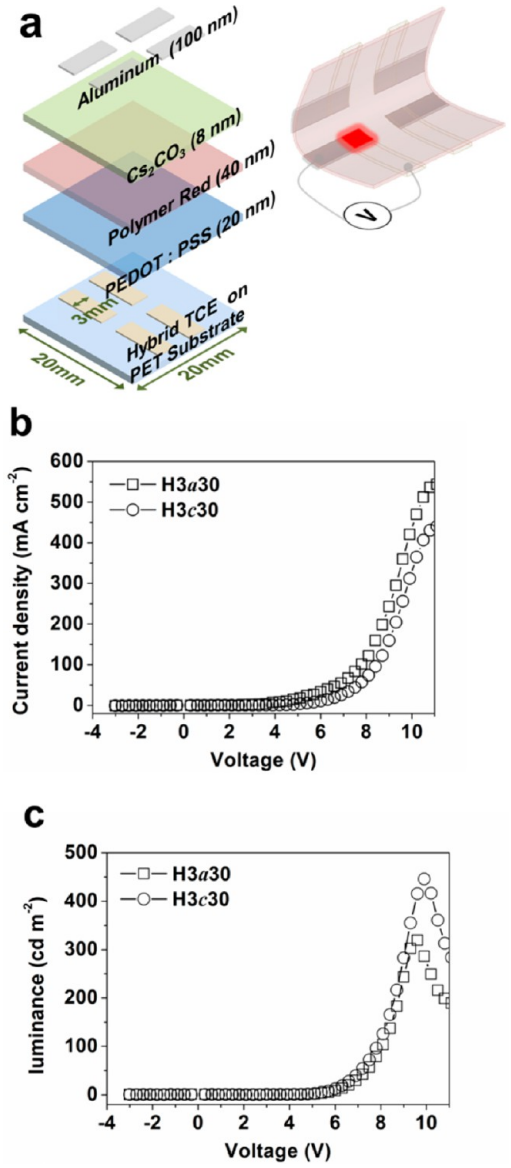

Figure 8. (a) Schematic descriptions of f-OLED structures, (b) *J*–*V* characteristics for f-OLEDs on the hybrid TCEs; H3*a*30 and H3*c*30, (c) luminance of f-OLEDs on H3*a*30 and H3*c*30.

substrate, which significantly reduces the junction resistance and the probability of separation of AgNWs by external stresses that induces electrical disconnection. The crystallinity of matrix and the adhesion between AgNWs and the matrix were found to be controlled by sputtering conditions and h_f. With the optimized crystallinity and adhesion strength, the hybrid TCEs were made not only more flexible but also more conductive than the AgNW networks. The transparency of the hybrid TCEs is also almost equivalent to that of AgNW networks. With composite with conductive polymers such as PEDOT:PSS, similar welding effect might be attained, but the polymer matrix degrades the lifetime of the electrode and devices. On the hybrid TCEs, f-OLEDs can be fabricated without top-coats, and the performances are equivalent or even better than those on commercial ITO. On the bare AgNW networks without top-coats, f-OLEDs have not been successfully fabricated because of electric shorts and the non-uniform quality of AgNWs over large areas. The success of f-OLEDs on the hybrid TCEs validates our proposal that the hybrid TCEs developed in this study can replace ITO in various flexible devices. The process–microstructure–property relationship of hybrid TCEs found in this study can be extended to hybrid TCEs welded with other matrix materials. We also make progress in further simplifying the process steps because the combination of solution- and dry-coating process may double the manufacturing cost and time.

AUTHOR INFORMATION

Corresponding Author

*E-mail: jwpark09@yonsei.ac.kr. Phone: +82 221235834. Fax: +82 221235834.

Notes

The authors declare no competing financial interest.

ACKNOWLEDGMENTS

This research was supported by a grant from the Fundamental R&D Program for the Technology of World Premier Materials (WPM), which is funded by the Ministry of Knowledge Economy, Republic of Korea.

REFERENCES

(1) Taylor, M. P.; Readey, D. W.; Van Hest, M. F. A. M.; Teplin, C. W.; Alleman, J. L.; Dabney, M. S.; Gedvilas, L. M.; Keyes, B. M.; To, B.; Perkins, J. D.; Ginley, D. S. The Remarkable Thermal Stability of Amorphous In-Zn-O Transparent Conductors. *Adv. Funct. Mater.* **2008**, *18*, 3169–3178.

(2) Hecht, D. S.; Hu, L.; Irvin, G. Emerging Transparent Electrodes Based on Thin Films of Carbon Nanotubes, Graphene, and Metallic Nanostructures. *Adv. Mater.* **2011**, *23*, 1482–1513.

(3) Ginley, D. S.; Bright, C. Transparent Conducting Oxides. *MRS Bull.* **2000**, *25*, 15–18.

(4) Cui, J.; Wang, A.; Edleman, N. L.; Ni, J.; Lee, P.; Armstrong, N. R.; Marks, T. J. Indium Tin Oxide Alternatives - High Work Function Transparent Conducting Oxides as Anodes for Organic Light-Emitting Diodes. *Adv. Mater.* **2001**, *13*, 1476–1480.

(5) Hosono, H.; Ohta, H.; Orita, M.; Ueda, K.; Hirano, M. Frontier of Transparent Conductive Oxide Thin Films. *Vacuum* **2002**, *66*, 419–425.

(6) Ohta, H.; Orita, M.; Hirano, M.; Tanji, H.; Kawazoe, H.; Hosono, H. Highly Electrically Conductive Indium-Tin-Oxide Thin Films Epitaxially Grown on Yttria-Stabilized Zirconia (100) by Pulsed-Laser Deposition. *Appl. Phys. Lett.* **2000**, *76*, 2740–2742.

(7) Kumar, A.; Zhou, C. The Race to Replace Tin-Doped Indium Oxide: Which Material Will Win? *ACS Nano* **2010**, *4*, 11–14.

(8) Alzoubi, K.; Hamasha, M.; Lu, S.; Sammakia, B. Bending Fatigue Study of Sputtered ITO on Flexible Substrate. *J. Display Technol.* **2011**, *7*, 593–600.

(9) Varela-Rizo, H.; Martín-Gullón, I.; Terrones, M. Hybrid Films with Graphene Oxide and Metal Nanoparticles Could Now Replace Indium Tin Oxide. *ACS Nano* **2012**, *6*, 4565–4572.

(10) Pang, S.; Hernandez, Y.; Feng, X.; Müllen, K. Graphene as Transparent Electrode Material for Organic Electronics. *Adv. Mater.* **2011**, *23*, 2779–2795.

(11) Wu, S.; Yin, Z.; He, Q.; Huang, X.; Zhou, X.; Zhang, H. Electrochemical Deposition of Semiconductor Oxides on Reduced Graphene Oxide-Based Flexible, Transparent, and Conductive Electrodes. *J. Phys. Chem. C* **2010**, *114*, 11816–11821.

(12) Wu, H.; Kong, D.; Ruan, Z.; Hsu, P. C.; Wang, S.; Yu, Z.; Carney, T. J.; Hu, L.; Fan, S.; Cui, Y. A Transparent Electrode Based on a Metal Nanotrough Network. *Nat. Nanotechnol.* **2013**, *8*, 421–5.

(13) Barnes, T. M.; Bergeson, J. D.; Tenent, R. C.; Larsen, B. A.; Teeter, G.; Jones, K. M.; Blackburn, J. L.; Van De Lagemaat, J. Carbon Nanotube Network Electrodes Enabling Efficient Organic Solar Cells without a Hole Transport Layer. *Appl. Phys. Lett.* **2010**, *96*, 243309.

(14) Hu, L.; Kim, H. S.; Lee, J. Y.; Peumans, P.; Cui, Y. Scalable Coating and Properties of Transparent, Flexible, Silver Nanowire Electrodes. *ACS Nano* **2010**, *4*, 2955−2963.
(15) Kim, C. H.; Cha, S. H.; Kim, S. C.; Song, M.; Lee, J.; Shin, W. S.; Moon, S. J.; Bahng, J. H.; Kotov, N. A.; Jin, S. H. Silver Nanowire Embedded in P3HT:PCBM for High-Efficiency Hybrid Photovoltaic Device Applications. *ACS Nano* **2011**, *5*, 3319−3325.
(16) Choi, D. Y.; Kang, H. W.; Sung, H. J.; Kim, S. S. Annealing-Free, Flexible Silver Nanowire-Polymer Composite Electrodes Via a Continuous Two-Step Spray-Coating Method. *Nanoscale* **2013**, *5*, 977−83.
(17) Gao, T.; Leu, P. W. Copper Nanowire Arrays for Transparent Electrodes. *J. Appl. Phys.* **2013**, *114*, 063107.
(18) Kiran Kumar, A. B. V.; wan Bae, C.; Piao, L.; Kim, S.-H. Silver Nanowire Based Flexible Electrodes with Improved Properties: High Conductivity, Transparency, Adhesion and Low Haze. *Mater. Res. Bull.* **2013**, *48*, 2944−2949.
(19) Li, Y.; Cui, P.; Wang, L.; Lee, H.; Lee, K.; Lee, H. Highly Bendable, Conductive, and Transparent Film by an Enhanced Adhesion of Silver Nanowires. *ACS Appl. Mater. Interfaces* **2013**, *5*, 9155−60.
(20) Yang, L.; Zhang, T.; Zhou, H.; Price, S. C.; Wiley, B. J.; You, W. Solution-Processed Flexible Polymer Solar Cells with Silver Nanowire Electrodes. *ACS Appl. Mater. Interfaces* **2011**, *3*, 4075−84.
(21) Lim, J.-W.; Cho, D.-Y.; Jihoon, K.; Na, S.-I.; Kim, H.-K. Simple Brush-Painting of Flexible and Transparent Ag Nanowire Network Electrodes as an Alternative ITO Anode for Cost-Efficient Flexible Organic Solar Cells. *Sol. Energy Mater. Sol. Cells* **2012**, *107*, 348−354.
(22) Coskun, S.; Selen Ates, E.; Unalan, H. E. Optimization of Silver Nanowire Networks for Polymer Light Emitting Diode Electrodes. *Nanotechnology* **2013**, *24*, 125202.
(23) Gaynor, W.; Burkhard, G. F.; McGehee, M. D.; Peumans, P. Smooth Nanowire/Polymer Composite Transparent Electrodes. *Adv. Mater.* **2011**, *23*, 2905−2910.
(24) Park, J.-W.; Lee, S.-H.; Yang, C.-W. Investigation of the Interfacial Adhesion of the Transparent Conductive Oxide Films to Large-Area Flexible Polymer Substrates Using Laser-Induced Thermo-Mechanical Stresses. *J. Appl. Phys.* **2013**, *114*, 063513.
(25) Kim, A.; Won, Y.; Woo, K.; Kim, C.-H.; Moon, J. Highly Transparent Low Resistance ZnO/Ag Nanowire/ZnO Composite Electrode for Thin Film Solar Cells. *ACS Nano* **2013**, *7*, 1081−1091.
(26) Zilberberg, K.; Gasse, F.; Pagui, R.; Polywka, A.; Behrendt, A.; Trost, S.; Heiderhoff, R.; Görrn, P.; Riedl, T. Highly Robust Indium-Free Transparent Conductive Electrodes Based on Composites of Silver Nanowires and Conductive Metal Oxides. *Adv. Funct. Mater.* **2014**, *24*, 1671−1678.
(27) Garnett, E. C.; Cai, W.; Cha, J. J.; Mahmood, F.; Connor, S. T.; Greyson Christoforo, M.; Cui, Y.; McGehee, M. D.; Brongersma, M. L. Self-Limited Plasmonic Welding of Silver Nanowire Junctions. *Nat. Mater.* **2012**, *11*, 241−249.
(28) Triambulo, R. E.; Kim, J. H.; Na, M. Y.; Chang, H. J.; Park, J. W. Highly Flexible, Hybrid-Structured Indium Tin Oxides for Transparent Electrodes on Polymer Substrates. *Appl. Phys. Lett.* **2013**, *102*.
(29) Kim, E. H.; Yang, C. W.; Park, J. W. The Crystallinity and Mechanical Properties of Indium Tin Oxide Coatings on Polymer Substrates. *J. Appl. Phys.* **2011**, *109*, 043511.
(30) Kim, H.; Gilmore, C. M.; Piqué, A.; Horwitz, J. S.; Mattoussi, H.; Murata, H.; Kafafi, Z. H.; Chrisey, D. B. Electrical, Optical, and Structural Properties of Indium-Tin-Oxide Thin Films for Organic Light-Emitting Devices. *J. Appl. Phys.* **1999**, *86*, 6451−6461.
(31) Park, J. W.; Kim, G.; Lee, S. H.; Kim, E. H.; Lee, G. H. The Effect of Film Microstructures on Cracking of Transparent Conductive Oxide (TCO) Coatings on Polymer Substrates. *Surf. Coat. Technol.* **2010**, *205*, 915−921.
(32) Belenkova, T. L.; Rimmerman, D.; Mentovich, E.; Gilon, H.; Hendler, N.; Richter, S.; Markovich, G. UV Induced Formation of Transparent Au-Ag Nanowire Mesh Film for Repairable OLED Devices. *J. Mater. Chem.* **2012**, *22*, 24042−24047.

NOTE ADDED AFTER ASAP PUBLICATION

Due to a production error, panels d and e for Figure 4 are not present in the version posted on the Web on April 18, 2014. The corrected version was reposted on May 1, 2014.